144 (2023) 213198

Contents lists available at ScienceDirect

Biomaterials Advances

journal homepage: www.journals.elsevier.com/materials-science-and-engineering-c

Facile post modification synthesis of copper-doped mesoporous bioactive glass with high antibacterial performance to fight bone infection

Maryam Hosseini [a,b,1], Negar Hassani Besheli [a,1], Dongmei Deng [c], Caroline Lievens [d], Yi Zuo [e], Sander C.G. Leeuwenburgh [a,*], Fang Yang [a,*]

[a] Department of Dentistry – Regenerative Biomaterials, Radboud Institute for Molecular Life Sciences, Radboudumc, Philips van Leydenlaan 25, 6525 EX Nijmegen, The Netherlands
[b] Department of Chemistry, Amirkabir University of Technology (Tehran Polytechnic), Tehran 1591634311, Iran
[c] Department of Preventive Dentistry, Academic Center for Dentistry Amsterdam, University of Amsterdam and Vrije Universiteit Amsterdam, Amsterdam 1081 LA, The Netherlands
[d] Department of Earth Systems Analysis, Faculty of Geo-information Science and Earth Observation, University of Twente, Hengelosestraat 99, 7514 AE Enschede, The Netherlands
[e] Analytic and Testing Center, Sichuan University, 610064 Chengdu, China

ARTICLE INFO

Keywords:
Post-modification
Sol-gel
Mesoporous bioactive glass nanoparticles
Copper
Antibacterial

ABSTRACT

Successful treatment of infected bone defects caused by multi-drug resistant bacteria (MDR) has become a major clinical challenge, stressing the urgent need for effective antibacterial bone graft substitutes. Mesoporous bioactive glass nanoparticles (MBGNs), a rapidly emerging class of nanoscale biomaterials, offer specific advantages for the development of biomaterials to treat bone infection due to endowed antibacterial features. Herein, we propose a facile post-modification sol-gel strategy to synthesize effective antibacterial MBGNs doped with copper ions (Cu-PMMBGNs). In this strategy, amine functional groups as chelating agents were introduced to premade mesoporous silica nanoparticles (MSNs) which further facilitate the incorporation of high content of calcium (~17 mol%) and copper ions (~8 mol%) without compromising nanoparticle shape, mesoporosity, and homogeneity. The resulting nanoparticles were degradable and showed rapidly induce abundant deposition of apatite crystals on their surface upon soaking in simulated body fluids (SBF) after 3 days. Cu-PMMBGNs exhibited a dose-dependent inhibitory effect on Methicillin-resistant *Staphylococcus aureus* (MRSA) bacteria, which are common pathogens causing severe bone infections. Most importantly, the nanoparticles containing 5 mol% copper ions at concentrations of 500 and 1000 $\mu g.mL^{-1}$ showed highly effective antibacterial performance as reflected by a 99.9 % reduction of bacterial viability. Nanoparticles at a concentration of 500 $\mu g.mL^{-1}$ showed no significant cytotoxicity toward preosteoblast cells (~85–89 % cell viability) compared to the control group. In addition, the nanoscale properties of synthesized Cu-PMMBGNs (~100 nm in size) facilitated their internalization into preosteoblast cells, which highlights their potential as intracellular carriers in combating intracellular bacteria. Therefore, these copper-doped nanoparticles hold strong promise for use as an antibacterial component in antibacterial bone substitutes such as hydrogels, nanocomposites, and coatings.

1. Introduction

Bone is a highly dynamic tissue that possesses an intrinsic potential to heal itself. However, this self-healing capability is substantially hindered by infection caused by e.g., open fractures and prosthetic materials [1]. Common modalities to treat bone infection including surgical debridement along with long-term systemic antibiotic therapy have not been sufficiently effective due to the low bioavailability of antibiotics and their reduced concentration at the infected site resulting from bone necrosis and vasculature damage [2,3]. Alternative approaches based on local drug delivery from implantable biomaterials have been developed to overcome the limitations of conventional treatments [4]. However, the therapeutic efficacy of these antibiotic-loaded bone substitutes remains limited to date due to i) a weak control over antibiotic release

* Corresponding authors.
E-mail addresses: Sander.leeuwenburgh@radboudumc.nl (S.C.G. Leeuwenburgh), Fang.yang@radboudumc.nl (F. Yang).
[1] These authors contributed equally to this work.

https://doi.org/10.1016/j.bioadv.2022.213198
Received 25 July 2022; Received in revised form 24 October 2022; Accepted 13 November 2022
Available online 16 November 2022

kinetics, ii) the invasive clinical application, and most importantly iii) the increased prevalence of multi-drug resistant (MDR) bacteria as a result of the widespread use of antibiotics [5,6]. These hard-to-treat pathogens such as Methicillin-resistant *Staphylococcus aureus* (MRSA) can induce severe bone infection and even intracellular persistence of these pathogens upon their invasion into host cells. Besides the limited therapeutic efficacy of currently available antibiotics against resistant bacteria, their low penetration into host cell plasma membranes increases the chance of recurrence of infection, which imposes an ever-increasing challenge for various surgical application areas [7,8]. Therefore, designing an effective antibacterial bone graft substitute is in urgent need to reduce the abundant usage of antibiotics to fight infected bone defects and relief the global concerns regarding resistant bacteria.

During the past decade, mesoporous bioactive glasses nanoparticles (MBGNs) have gained considerable interest for application in bone-regenerative surgery owing to their excellent functional properties including their evident apatite-forming ability, antibacterial, and osteopromotive properties [9,10]. The highly ordered mesostructured channels and ultrahigh surface area (>100 m^2/g) allow for high loading and controlled release of therapeutic ions. Moreover, their nanometric size facilitates internalization by cells, which opens new opportunities to target intracellular bacteria. The presence of calcium ions substantially improves their bioactivity and increases the glass dissolution rate by acting as a network modifier [9,11]. The intrinsic antibacterial property of bioactive glass has been generally attributed to the release of alkali ions like calcium which affect the local biological environment (pH and osmolarity) inhibiting bacterial growth [9]. However, the intrinsic antibacterial capacity of bioglass is often limited [12]. Therefore, various therapeutic ions have been incorporated into bioglass to boost their antibacterial performance even further [9,13]. Among them, copper ions (Cu^{2+}) possess robust and broad-spectrum bactericidal activity as well as angiogenic and osteogenic properties [14]. However, only limited studies have been reported on the antibacterial efficacy of copper-doped MBG in the form of nanoparticles. Bari et al. demonstrated a moderate antibacterial efficiency (50–75 %) of these nanoparticles synthesized by ultrasound-assisted sol-gel procedure against various bacteria including *Staphylococcus aureus*, *Staphylococcus epidermidis*, and *Escherichia coli*, but therapeutic efficacy against resistant bacteria has not yet been shown [15]. Therefore, the design of Cu-MBGNs with strong bactericidal efficacy against resistant bacteria would offer new opportunities to fight infected bone defects using an antibiotic-free antibacterial biomaterial approach.

Various methods have been reported to produce MBGNs doped with therapeutic ions. The microemulsion-assisted sol-gel method is one of the most commonly studied synthesis routes [16–20]. However, this method is typically associated with heterogeneity in particle size and shape due to the fusion and deformation of microemulsion droplets. More importantly, the incorporation of high contents of metallic ions using this method is challenging, since changes in ionic concentrations induce particle aggregation resulting in uncontrollable particle sizes [20,21]. This shortcoming may severely compromise the therapeutic efficacy of MBGNs such as their bactericidal effects. Post-modification sol-gel approaches offer more control over the dispersity and shape of nanoparticles since metal ions are added after the formation of premade silica nanoparticles [22–24] or binary (mesoporous) bioactive glass nanoparticles [21,25]. However, introducing high contents of ions into the silica network still remains a challenge due to the presence of limited active sites (-SiOH) on premade silica nanoparticles. Additionally, control over ion release is typically poor due to the weak bonds between active sites and metallic ions [21]. We propose that introducing new active sites with a strong affinity for metal ions will increase the capacity of particles to store large amounts of antibacterial ions to combat resistant bacteria efficiently. The strong affinity between amine groups and heavy metals (e.g., Cu^{2+} and Fe^{2+}) has been previously implemented for water purification applications. [26,27]. In addition, the conjugation of amine groups into mesoporous silica nanoparticles (MSNs) is a commonly applied strategy for drug loading or target delivery [28–30]. However, introducing amine groups into MSNs to convert these inert nanocarriers into bioactive nanoparticles with antibacterial properties has not been reported yet.

Therefore, with this new sight, we envisaged that homogeneously sized and shaped MBGNs with a high capacity to adsorb ions (Ca^{2+} and Cu^{2+}) can be obtained by conjugation of amine groups as new active sites to premade MSNs. In more detail, we attempted to introduce these amine groups to the inner pore area of premade MSNs to allow the diffusion of ions into the particle interior and obtain improved control over ion release. This approach offers several advantages over the conventional microemulsion-assisted sol-gel method. Firstly, this post-modification method offers better control over particle dispersity since the premade particles are used for the doping process. For the same reason, this approach provides a versatile platform by which a wide range of MBGNs with various sizes, compositions, and (pore) morphologies (such as hollow structures) can be produced depending on the requirements of specific applications. Secondly, due to the presence of amine groups in the inner and outer parts of the particles, incorporation of high content of ions without forming any metal oxide crystals will be more feasible compared to the conventional approach in which particle aggregation commonly occurs by increasing ionic content. In addition, the synthesized particles can be more tailorable in terms of degradability due to the presence of high content of ions in the silica network. Here, we demonstrated the synthesis of three groups of MBGNs (~100 nm) enriched with calcium and copper using this facile post-modification approach. Subsequently, the chemical, structural, morphological, and biological properties in terms of mineral-forming capacity, antibacterial performance, cytocompatibility, and internalization capacity of synthesized particles were studied in detail. A favorable apatite forming ability along with an effective antibacterial performance of Cu-PMMBGNs and their internalization ability (5 % mole) highlight the potential of these nanoparticles as an antibacterial component in antibacterial bone substitutes such as hydrogels, nanocomposites, and coatings.

2. Materials and methods

2.1. Materials

All reagents were used without further purification unless stated otherwise.

2.2. Synthesis of XCu-PMMBGNs

The synthesis route is shown in Scheme 1. Mesoporous silica nanoparticles (MSNs) were first synthesized according to the sol-gel method as reported in the literature [28]. Briefly, cetyltrimethylammonium bromide ($C_{19}H_{42}BrN$, CTAB, 0.5 g) was dissolved in a solution containing deionized water (240 mL) and sodium hydroxide (NaOH, 1.75 mL, 2 M) and then left under vigorous stirring at 80 °C for 2 h. Afterward, tetraethyl orthosilicate ($SiC_8H_{20}O_4$, TEOS, 2.5 mL) was added dropwise to react for another 2 h. The collected product was thoroughly washed with ethanol and water and finally dried as a white powder. In the next step, ion exchange extraction was used to remove the organic template before amine functionalization. In summary, 1 g of the dried sample was dispersed in an ethanolic solution of ammonium nitrate (NH_4NO_3, 100 mL, 10 $mg.mL^{-1}$) and refluxed for 6 h at 80 °C. The final product was dried after being thoroughly washed with ethanol. A predominantly spherical-to-oval shape morphology of the nanoparticles, i.e. MSNs, could be observed with an average size of 107 ± 16 nm (Fig. S1A-C). FTIR analysis (Fig.S1D) confirmed the CTAB removal as evidenced by the disappearance of the aliphatic C—H stretching vibration at 2900 cm^{-1}.

To prepare amine-functionalized MSNs (NH_2MSNs), aqueous dispersion of MSN (10 $mg.mL^{-1}$) reacted with (3-Aminopropyl)

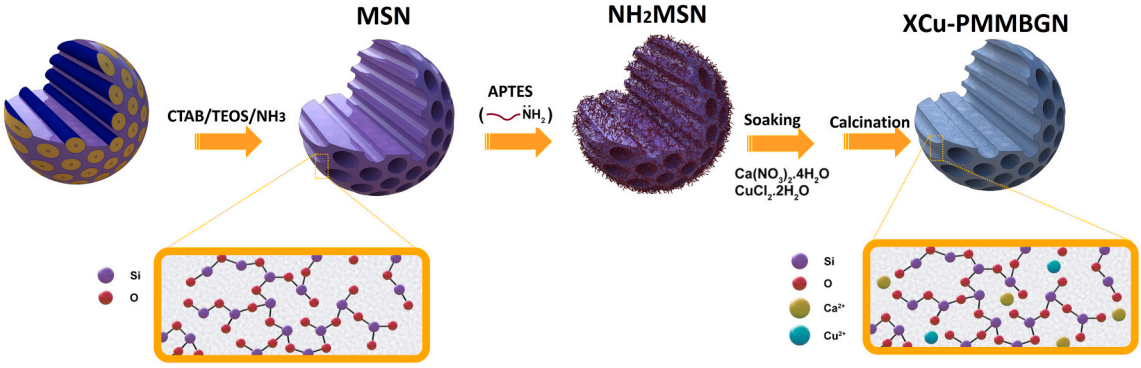

Scheme 1. Schematic illustration describing the synthesis of MBGNs by the proposed post-modification approach.

triethoxysilane (APTES, 0.43 mM) under stirring for 36 h at room temperature. Afterward, the reaction was heated for 2 h at 80 °C. The white precipitate was collected by centrifugation and washed several times with ethanol before the drying process. To prepare bioactive glass nanoparticles, an optimized post-modification method was employed. Calcium nitrate tetrahydrate ($Ca(NO_3)_2.4H_2O$, denoted as CaN) and copper (II) chloride dihydrate ($CuCl_2.2H_2O$) were used as Ca and Cu precursors. To this end, an aqueous well-dispersed MSNs and NH_2MSNs dispersion with the predetermined silica content were soaked in various amounts of CaN to achieve different Ca: Si precursor molar ratios (1:1, 1.5:1, 2:1, 4:1, and 8:1).

After 30 min of stirring, the particles were centrifuged, dried, and then subjected to calcination to incorporate the adsorbed Ca ions into the silicate network forming MBGNs (680 °C, 3 h, a heating rate of 2 K.min^{-1}). To remove the excess amount of calcium precursor, the resulting particles were thoroughly washed with ethanol. To prepare XCu-PMMBGNs (X = 2, 5 mol% of Cu), Cu was substituted with 2 and 5 mol% of Ca. To produce copper-containing hollow mesoporous bioactive glass nanoparticles, hollow mesoporous silica nanoparticles were first produced via a selective etching approach [31]. Then, the same amine modification and soaking process were applied to introduce Ca and Cu ions to the premade hollow mesoporous silica nanoparticles.

2.3. Synthesis of MBGNs by microemulsion-assisted sol-gel method

For comparison reasons, the conventional microemulsion-assisted sol-gel method was applied to synthesize MBGNs with some modifications [17,20]. A binary SiO_2-CaO composition was prepared using Ethyl acetate (EA)-CTAB-water microemulsion droplets as a soft template. CTAB (0.56 g) was dissolved in deionized water (26 mL) under continuous stirring to obtain a clear solution. Then EA (8 mL) was added to start the droplet formation. After 30 min, ammonium hydroxide (28 %) was added dropwise to adjust the pH to around 10.5. After 15 min, TEOS and CaN were added at different Ca: Si precursor molar ratios every 30 min intervals to find out the maximum achievable Ca incorporation into the silica network. To this end, 3 mL of TEOS and 2.21, 3.1, 4.6, and 6.2 g of CaN were added to achieve Ca: Si molar ratios of 0.7:1, 1:1, 1.5:1, and 2:1, respectively. After 4 h of mixing, the resulting white precipitation was collected by centrifugation and washed with water and ethanol three times before the drying step. Afterward, the organic template and nitrates were removed by calcination of dry powders at 680 °C for 6 h with a heating rate of 2 K.min^{-1}.

2.4. Physicochemical characterization of particles

Detailed information regarding nanoparticle characterization was included in the supporting information section. Briefly, the morphology and mesostructure of all synthesized nanoparticles were visualized by Scanning Electron Microscope (SEM) and Transmission Electron Microscope (TEM), respectively. The average size and size distribution of particles were determined by measuring the diameter of at least 100 particles using ImageJ software. The hydrodynamic size and zeta potential of particles were measured using Dynamic Light Scattering (DLS) and Laser Doppler Electrophoresis, respectively. SEM equipped with an energy dispersive X-ray detector (EDX) as well as Inductively Coupled Plasma Optical Emission Spectroscopy (ICP-OES) were employed to analyze the elemental composition of particles. Elemental distribution in nanoparticles was visualized by TEM equipped with EDX. Fourier Transform Infrared Spectroscopy (FTIR) and Powder X-ray diffraction (XRD) analyses were carried out to study the particle structures. The specific surface area and pore size distribution of nanoparticles were analyzed using nitrogen adsorption-desorption analysis. Additionally, a ninhydrin colorimetric assay was performed to confirm the amine functionalization procedure.

2.5. Release study

The time-dependent dissolution behavior of synthesized XCu-PMMBGNs (X = 2, 5 mol% of Cu) was evaluated in two different media including SBF and alpha Minimum Essential Medium (α-MEM) supplemented with 10 % fetal bovine serum (FBS) at pH 7.4. Nanoparticles (20 mg) were dispersed in culture media (3 mL) then the dispersion was placed in a dialysis tube (3.5 K MWCO, 16 mm dry I.D; Thermo Fisher Scientific, UK) and immersed in a polypropylene bottle containing culture media (17 mL). The samples were incubated at 37 °C under 120 rpm shaking for different time points (1, 3, 5, 24, 48, 120, 168, and 336 h). At the end of each time interval, half of the bulk solution was taken out and then replaced with the same volume of fresh media. The same dissolution study was performed in SBF. The collected aliquots were then diluted using nitric acid solutions (2 v/v%) and analyzed by ICP-OES to determine the concentration of Si, Ca, and Cu ions in the supernatants.

2.6. In vitro bioactivity assessment

To evaluate the apatite-forming ability of XCu-PMMBGNs (X = 0, 2, 5 mol% of Cu), particles were immersed in simulated body fluid (SBF) prepared according to the reported protocol in the literature [32,33]. Briefly, nanoparticles (20 mg) were soaked in SBF (20 mL) at 37 °C under shaking at 120 rpm for up to 14 days. SBF was not refreshed and at each predetermined time interval (1, 3, 7, and 14 days), the particles were collected and rinsed three times with deionized water before drying. The formation of the apatite-like phase was assessed by SEM, TEM, FTIR, and XRD analyses. The change in pH and the concentrations of Si, Ca, and Cu ions in the supernatant were also monitored at each time interval.

2.7. In vitro antibacterial properties of nanoparticles

2.7.1. Bacterial strain, culture conditions, and sample preparation

MRSA bacteria were cultured in 5 mL of Brain Heart Infusion (BHI) broth from frozen stock and incubated at 37 °C overnight under 150 rpm shaking. Subsequently, the concentration of bacterial suspension was adjusted to a 1×10^4 colony-forming unit ($CFU.mL^{-1}$) for further steps. Different groups of nanoparticles were first autoclaved at 120 °C and then evenly dispersed in sterile PBS at a final concentration of 2 mg. mL^{-1} using a bath sonicator for 15 min. Furthermore, different dilutions of nanoparticles were properly prepared in concentrated BHI broth to obtain particle concentrations of 31.25, 62.5, 125, 250, 500, and 1000 $\mu g.mL^{-1}$.

2.7.2. Evaluation of antibacterial properties of nanoparticles

Bacteria were exposed to the nanoparticle dispersion with different concentrations in 96 well plates and incubated at 37 °C. To study the effect of nanoparticles on bacterial growth kinetics, the optical density (OD) of the bacterial culture was monitored at a wavelength of 600 nm every 30 min for 24 h in a spectrophotometer. The wells containing bacterial cells without nanoparticles served as negative controls. Vancomycin (8 $\mu g.mL^{-1}$) was included as a positive control since MRSA bacteria used in this study were sensitive to this antibiotic. It should be also noted that nanoparticle dispersion in BHI broth specifically at high concentrations resulted in a slurry dispersion. Therefore, the OD_{600} reading of nanoparticle dispersion was subtracted from the final OD_{600} readings of each related well to avoid any interference.

Furthermore, a resazurin reduction assay was performed to evaluate the effect of each group of nanoparticles on bacterial cell viability. Resazurin is a weakly fluorescent dye that can be reduced to a highly fluorescent resorufin by oxidoreductases within metabolically active cells. The quantity of generated resorufin is considered proportional to the number of viable bacterial cells. After 24 h of incubation of bacterial cells with nanoparticles, resazurin was added to each well at the final concentration of 0.0016 % w/v. The 96-well plates were incubated at 37 °C for 30 min. The relative fluorescent unit (RFU) of generated resorufin was measured at λex = 485 nm/λem = 580 nm in a microplate reader.

2.8. In vitro cytotoxicity assay

The cytotoxicity of XCu-PMMBGNs (X = 0, 2, 5 mol% of Cu) was assessed using a calorimetric CCK8 assay. Preosteoblast MC3T3-E1 cells were seeded in flat-bottomed 96-well plates, at a seeding density of 5×10^4 $cells.mL^{-1}$ in basal α-MEM media supplemented with 10 % fetal bovine serum (FBS) (v/v), 100 $U{\cdot}mL^{-1}$ penicillin, and 100 $\mu g{\cdot}mL^{-1}$ streptomycin at 37 °C in a humidified incubator equilibrated with 5 % CO_2 for 24 h. Nanoparticles were sterilized by autoclave at 120 °C for 45 min and subsequently evenly dispersed and incubated in culture media concentrations of 1000 $\mu g.mL^{-1}$ for 24 h. Then, the nanoparticles were collected by centrifuge (12,000 rpm, 30 min) and the media was refreshed. When cells reached 70–80 % of confluency, culture media was replaced with fresh basal media containing nanoparticles at different concentrations (500 and 1000 $\mu g.mL^{-1}$) and incubated for 1 and 3 days. Cells growing in the basal medium without nanoparticles were considered as control. After each time point, the media containing nanoparticles were removed and cells were washed with PBS. Then 200 μL of fresh basal media containing CCK8 (10 % v/v) reagent was added to each well followed by 4 h of incubation at 37 °C. Afterward, the optical density (OD) values of the cells were measured at 450 nm using a microplate reader.

Cell survival was also assessed using the LIVE/DEAD™ Viability/Cytotoxicity kit (Invitrogen molecular probes, Eugene, USA). Cells were seeded at a density of 10,000 $cells/cm^2$ in a surface-treated μ-slide 8 well (ibidi) and incubated overnight to adhere. Then 5Cu-PMMBGNs at concentrations of 500 and 1000 $\mu g.mL^{-1}$ were added to the cells and incubated for 1 and 3 days. After each time point, the media containing nanoparticles was removed and the cells were incubated with a working solution (approximately 2 μM calcein AM and 4 μM EthD-1 in D-PBS) for 30 min at 37 °C. Afterward, the samples were visualized with fluorescence microscopy (Carl Zeiss, Gottingen, Germany).

2.9. Internalization of 5Cu-PMMBGNs

In order to monitor the cellular uptake of 5Cu-PMMBGNs, the nanoparticles were first fluorescently labeled. To this end, FITC-APTES conjugate was prepared by dissolving FITC (2.5 μM) in 5 mL dimethyl sulfoxide followed by the addition of APTES (2.5 μM) and mixing for 1 h at room temperature. Then the prepared conjugate was added to the 100 mL well-dispersed nanoparticle dispersion in toluene (1 mg/mL). The reaction was kept stirring at 70 °C overnight. Subsequently, the labeled nanoparticles were thoroughly washed with ethanol and water through 5 centrifugation and redispersion steps.

To visualize the internalization of 5Cu-PMMBGNs, cells were seeded on Ibidi μ-slide 8-well plates at a density of 1.0×10^4 $cells/cm^2$ (MC3T3-E1). Final confluency of approximately 50 % was ensured to minimize overlapping cells. Afterward, cells were stained with 1 μM CellTrace™ yellow (Invitrogen) in PBS according to the manufacturer's instructions. Then, cells were exposed to a 200 μL growth medium containing 25 μg/mL of nanoparticles for 24 h. Post-exposure, cells were washed with PBS and stained with 50 nM LysoTracker in phenol red-free Roswell Park Memorial Institute medium (RPMI, Gibco) supplemented with 10 % FBS and 20 mM HEPES (Sigma-Aldrich) 30 min before imaging. Images were captured by Leica TCS SP8 SMD (Leica Microsystems) equipped with a temperature-controlled stage at 36.5 °C.

2.10. Statistical analysis

The elemental analyses, ion release study, textural properties, cell viability, and antibacterial studies were carried out at least in triplicate and all values were expressed as mean ± standard deviation (SD). Statistical analysis of the in vitro tests was evaluated using a one- or two-way analysis of variance (ANOVA) test, followed by Tukey's test (GraphPad Prism 8.4.3), and $*p < 0.05$ was considered statistically significant.

3. Results and discussion

3.1. Fabrication process and characterization

We introduced a facile post-modification strategy to fabricate antibiotic-free antibacterial MBGNs with homogenous size and shape along with a high capacity to store metallic ions (Scheme 1) addressing the common issues in the microemulsion-assisted sol-gel method. MSNs were firstly synthesized via a modified Stöber method and then functionalized with amine groups (NH_2MSNs) as active anchoring sites to increase the absorption capacity of metallic ions in the following soaking process. Therefore, the applied template i.e., CTAB was first removed from the premade MSN to create the mesostructure and increase the accessibility of active sites i.e., silanol groups inside the pores for further amine modification [28]. The resulting MSNs exhibited a large specific surface area of about 788 m^2/g and a narrow pore size distribution centered at 3.1 nm confirming the mesoporosity (Fig. S1E–F, and Table S1). After introducing amine groups using APTES, a new peak at ~1640 cm^{-1} appeared in the FTIR spectrum (Fig. S1D), which corresponds to the bending vibration of the N—H bond, indicating successful conjugation of amine groups [28]. Moreover, as shown in Fig. S1E and Table S1, a significant reduction in the specific surface area of particles was observed after the amine functionalization which can be attributed to the blocking effect of grafted APTES in the mesoporous channels [34,35]. This reduction along with a high content of primary amine groups (~45 wt%) determined by colorimetric ninhydrin assay

confirmed the coverage of large parts of the MSNs surface by amine groups. These amine groups also induced a change in nanoparticle surface charge from −25.1 to +11.8 mV (Table S1). To impart bioactivity (in terms of mineral-inducing capacity) to silicate-based biomaterials and enhance their dissolution rate, Ca ions were incorporated into the silicate structures as network modifiers. Of note, even though Ca ions can only adsorb on the surface of nanoparticles during the soaking process, they incorporate into the silicate network at high temperatures during calcination, leading to the formation of MBGNs [36]. We, first, investigated the effect of amine groups present in the large part of the nanoparticles on the maximum achievable incorporated Ca content at different applied Ca:Si molar ratios. Fig. 1A shows the Ca incorporation as a function of Ca:Si ratio in which at low Ca:Si ratios, PMMBGNs obtained from premade NH_2MSNs (PMMBGNs (NH_2MSN)) showed similar incorporated Ca contents as PMMBGNs obtained from premade MSNs (PMMBGNs (NH_2MSN)), although premade NH_2MSNs had a significantly lower surface area (Table S1) and subsequently lower amounts of accessible silanol groups compared to MSNs. This result highlights the effect of amine groups which could facilitate Ca adsorption, compensating for the limited surface area of NH_2MSNs. In both samples, higher Ca:Si ratios resulted in higher Ca incorporation but different crystalline phases of Ca crystals formed concomitantly as shown in the corresponding XRD patterns (Fig. 1B–C) [37–39]. Therefore, MBGNs with a Ca content up to ~17 % (measured by ICP, in 1.5:1 Ca:Si ratio) were fabricated using the proposed post-modification method.

We investigated the maximum achievable calcium content with preserved particle homogeneity using a common microemulsion-assisted sol-gel approach (Fig. 2A). MBGNs with spherical morphology and size of 100 nm with radial shape mesostructure were produced as shown in Fig. 2B–D. A maximum incorporated calcium content of 13.4 % (Fig. 2E, measured by ICP) was achieved with microemulsion approach which is in line with similar reported values [16,21,40,41]. This value was achieved by controlling the Ca: Si precursor molar ratio (Fig. S2). We showed that in the common approach, exceeding a threshold value of the Ca:Si precursor of 1.5:1 not only led to the formation of abundant small clusters around the nanoparticles and agglomeration of the final product but also reduced the calcium incorporation. Higher incorporated calcium content obtained in the post-modification strategy could be attributed to the different absorption sites for Ca^{2+} ions. In this proposed method, at the early stage of the soaking process, the concentration gradient of metal ions presents in bulk solution and active sites of NH_2MSNs (-SiOH and $-NH_2$ groups) led to the diffusion and absorption of metal ions more effectively. However, in the microemulsion-assisted sol-gel method, the presence of a template that occupies the pores along with several washing steps to remove non-reacted precursors, reduced the capacity of adsorbed ions [40].

Next, to enhance the intrinsic antibacterial properties of PMMBGNs, Cu ions with proven bactericidal ability were incorporated into the silica network as the second network modifier. Thereafter, copper ion-containing PMMBGNs denoted as XCu-PMMBGNs (X is incorporated

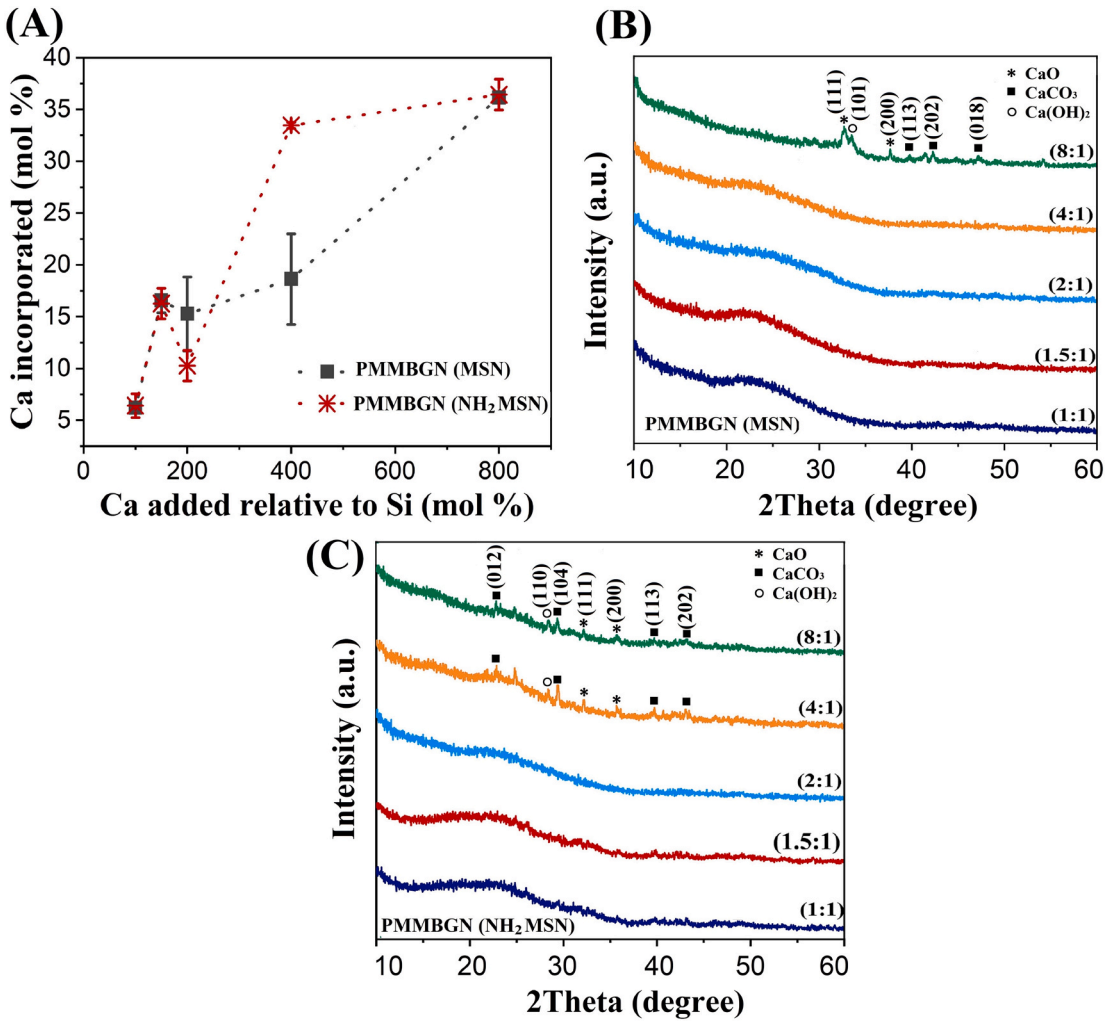

Fig. 1. Optimization of calcium content in PMMBGNs using post-modification approach. A) Incorporated calcium content as a function of Ca:Si precursor ratio. B) and C) XRD patterns of obtained PMMBGNs produced by premade MSNs and NH_2MSNs with different applied Ca:Si ratios, respectively.

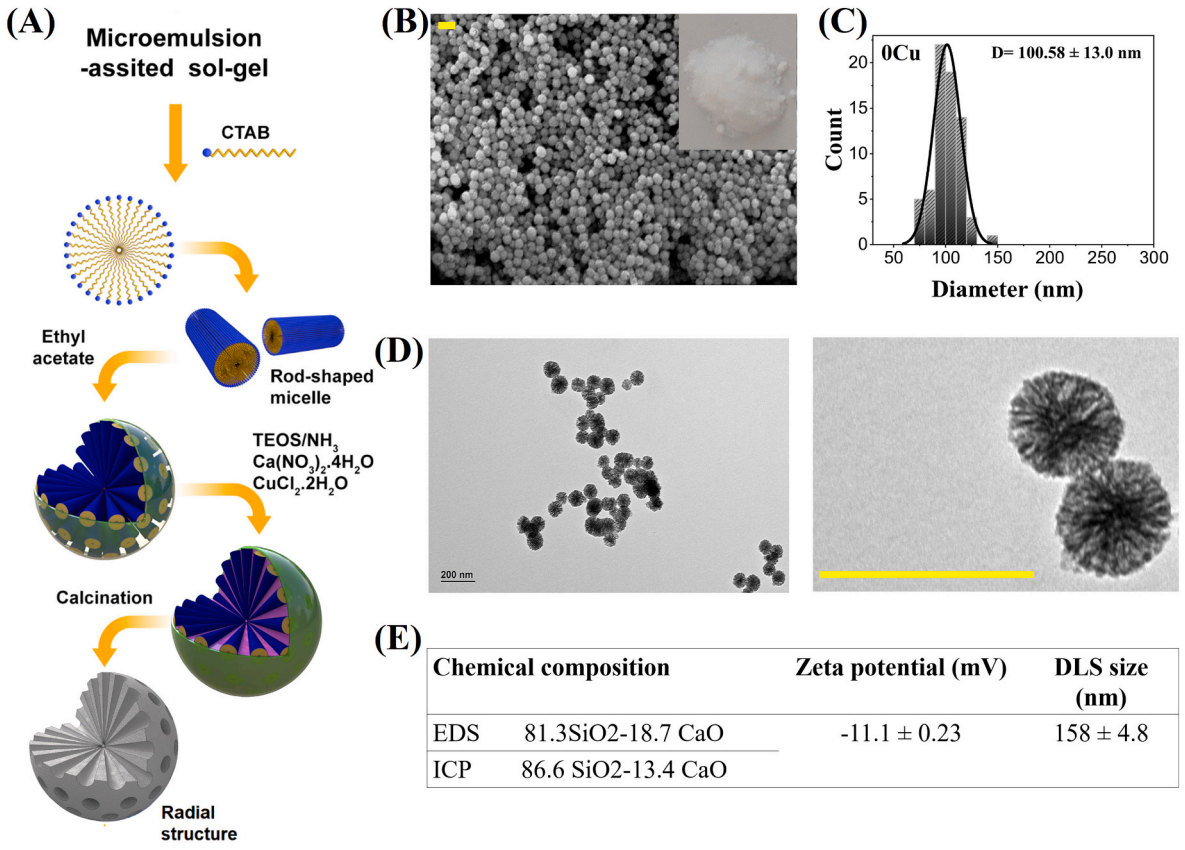

Chemical composition		Zeta potential (mV)	DLS size (nm)
EDS	81.3SiO2-18.7 CaO	-11.1 ± 0.23	158 ± 4.8
ICP	86.6 SiO2-13.4 CaO		

Fig. 2. Synthesis and optimization of MBGNs through the microemulsion-assisted sol-gel method. A) Synthesis route, B) SEM image, and C) size distribution of synthesized nanoparticles. D) TEM image and E) chemical composition and surface properties of synthesized nanoparticles. Scale bars in panels B and D represent 200 nm.

Cu content of 0, 2, and 5 mol%.), were fabricated using the optimized Ca: Si ratio (1.5: 1). We confirmed that the presence of amine groups resulted in considerably higher incorporated Cu contents. For example, 4.8 mol% of copper was successfully incorporated into NH_2MSNs by adding only 0.012 w/w% of copper chloride to NH_2MSNs powder, while adding more copper precursor (7 times higher) resulted only in 1.35 mol % of copper in MSNs samples (Table S2). The intensified blue color in the collected 2Cu-NH_2MSNs compared to 2Cu-MSNs sample shown in Fig. 3A highlights the higher affinity between copper and amine groups present in the particle structure. This strong affinity led to a high loading content of Cu ions into the silicate network of up to 8 % without crystal formation (Fig. S3). Zhang et al. reported a maximum incorporated content of copper of about 6.1 % into MBGNs with no sign of Cu-based crystalline nanoparticles by the microemulsion-assisted sol-gel method. However, an ascorbic acid/Cu complex was applied as the precursor of copper to reach this maximum value, which resulted in the heterogeneous size distribution of nanoparticles between 100 and 300 nm [20].

Fig. 3B shows the possible interactions between metallic ions and the silica surface before and after amine functionalization. For MSN, metallic ions (Ca^{2+} and Cu^{2+}) are likely adsorbed on the silica surface through ion exchange and chelation via hydroxyl groups, while for NH_2MSNs, amine groups also facilitate this adsorption through chelation via the electron pair in nitrogen [42,43]. This high affinity could also be attributed to the formation of a coordination complex between Cu^{2+} possessing d9 electron configuration with N- and O-donor ligands in amine and silanol groups, respectively. It can be concluded that amine groups induced copper incorporation more effectively than calcium incorporation. This can be attributed to the higher charge-to-radius ratio for Cu (Z/r Cu^{2+} = 2.74 $Å^{-1}$) compared to Ca (Z/r Ca^{2+} = 2.02 $Å^{-1}$), leading to the formation of stable complexes with electron donor functional groups i.e., –SiOH and –NH_2 surface groups [26,27]. Indeed, further research has to be conducted to confirm our proposed mechanism.

Fig. 3C shows the final morphology of synthesized XCu-PMMBGNs visualized by SEM in which nanoparticles have homogenous size and shape. The TEM image displays visible parallel pore structures in the obtained nanoparticles (Fig. 3D). The presence and distribution of Si, Ca, and Cu ions in 5Cu-PMMBGNs are confirmed by their corresponding elemental mapping shown in Fig. 3E. Table 1 lists the chemical compositions, textural, and surface properties of XCu-PMMBGNs. According to this table and Fig. ioS4, the incorporation of Ca and Cu ions did not induce a noticeable change in either the particle size in both dry and hydrodynamic states or the pore size. Therefore, we hypothesized that the proposed post-modification method would allow us to produce MBGNs with various sizes and (pore) morphologies. As a proof of concept, copper-containing hollow mesoporous bioactive glass nanoparticles with a size of 177 ± 22 nm and chemical composition of 87.34 SiO2-8.73 CaO-4.03 CuO were synthesized by a similar soaking process (Fig. S5). This structure with a low density of silica could be considered a safe drug carrier with low toxicity.

We further analyzed the molecular glass structure of XCu-PMMBGNs using FTIR analysis. The spectra show characteristic bands of the silicate glasses located at ~450 and ~800 cm^{-1} assigned to Si–O–Si bending and symmetric stretching vibrations, respectively (Fig. S6). A weak shoulder appeared at ~950 cm^{-1} corresponding to the stretching mode of Si–O–NBO (non-bridging oxygen bonds). The amorphous structure of all samples was confirmed by their XRD patterns, as only one broadband located at $2\theta = 23°$ was observed (Fig. S6) [20,21]. It should be noted that a similar glass structure was observed for the obtained MBGNs synthesized by the microemulsion method as depicted in Fig. S7. Taken together, firstly, the post-modification strategy succeeded to overcome the challenges reported in the common microemulsion method,

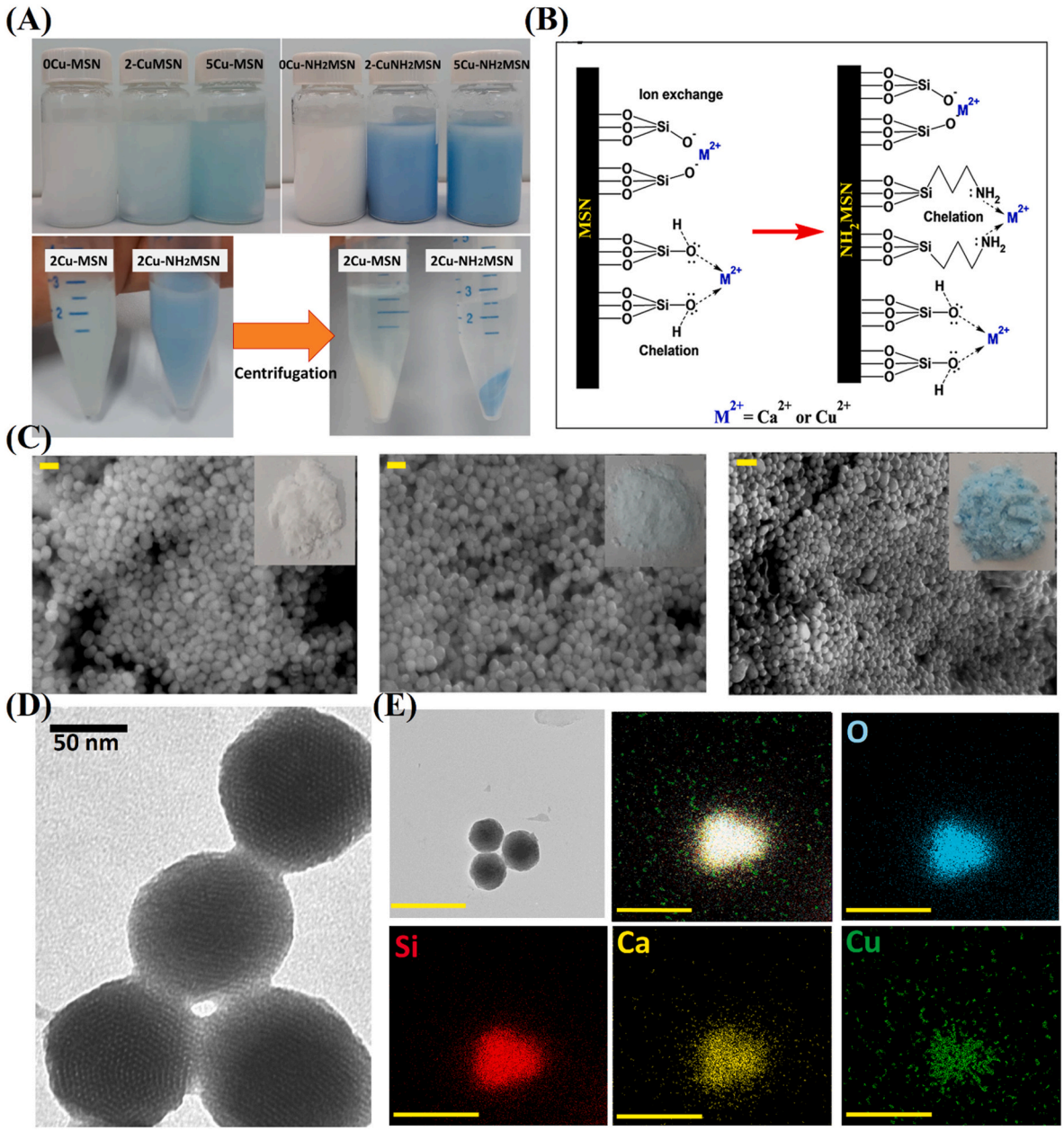

Fig. 3. Fabrication and characterization of XCu-PMMBGNs. A) Optical images of XCu- MSN and XCu- NH_2MSN (0, 2, and 5 % of Cu) after soaking confirm the strong affinity between amine groups and copper ions. B) Proposed mechanism for the incorporation of metallic ions into aminated particles. C) SEM and optical images (insert) of XCu-PMMBGNs (0, 2, and 5 % of Cu). D) TEM images and E) elemental distribution in 5Cu-PMMBGNs. Scale bars represent 200 nm in panels C and E. (For interpretation of the references to color in this figure, the reader is referred to the web version of this article.)

Table 1
Chemical compositions, textural and surface properties of synthesized XCu-PMMBGNs. SSA refers to the specific surface area of the nanoparticles.

Samples	Chemical composition (mol%)		Zeta potential (mV)	DLS size (nm)	SSA (m^2/g)	Pore volume (cm^3/g)	Pore size (nm)
XCu-PMMBGNs							
0 Cu	EDX	83.7 SiO_2-16.3 CaO	−7.3 ± 0.81	175 ± 10.1	49	0.11	3.48
	ICP	83.3 SiO_2-16.7 CaO					
2 Cu	EDX	88.5SiO_2-11.5CaO-2.7CuO	−10.3 ± 0.47	172 ± 4.9	99	0.14	3.13
	ICP	86.8 SiO_2-11.9 CaO-1.5 CuO					
5Cu	EDX	89.5 SiO_2-10.5 CaO-4.8CuO	−10.8 ± 0.6	170 ± 8.5	77	0.09	3.16
	ICP	87.8 SiO_2-8.0 CaO-4.2 CuO					

including the low control over the particle dispersity and low metal ions loading in MBGNs fabrication. Secondly, as in this strategy, ion loading did not affect the size and morphology of the premade nanoparticles, this synthesis route can be considered a versatile platform that allows for the synthesis of a wide range of compositions, sizes, and morphologies of bioglasses. Next, we evaluated the performance of synthesized XCu-

PMMBGNs (0, 2, and 5 mol%), by assessing their mineralization capacity, dissolution behavior, antibacterial performance, cytotoxicity, and cellular uptake.

3.2. Ion release by nanoparticles

The release profile of various ions from synthesized XCu-PMMBGNs was measured in SBF and α-MEM for up to 14 days. As shown in Fig. 4A, the first stage of Si dissolution corresponds to the disruption of the outer layer of the silica network, giving rise to an initial fast release. This fast release was then followed by a more gradual Si release for up to 14 days. The biodegradability of XCu-PMMBGNs was confirmed by 36–45 % release of initial silica ions in the nanoparticles (Fig. S8). This could be attributed to particle porous structure and pH rise during immersion in media that facilitate the hydrolysis and breakage of Si-O-Si bondages [44]. Unexpectedly, an initial fast release of Cu ions for 1 day occurred followed by a slow release until day 5 (Fig. 4B). Even though conjugation of amine groups guided the copper ions to the inner parts of the nanoparticle during the soaking process and subsequently localized them to the inner layers of nanoparticles after the calcination process, copper ions could escape the pores easily due to the small size (~0.1 nm) compared to the pore size (~3 nm) of nanoparticles. Regarding Ca ions, a significantly reduced release rate after 24 h was observed in SBF, which confirmed a fast deposition of calcium phosphate (Fig. 4C). Immersion of PMMBGNs in SBF containing a high level of Ca (84.73 $mg.L^{-1}$ in SBF) could accelerate ion exchange, leading to a rapid supersaturation and consequently fast calcium phosphate precipitation [45]. The release of all ions from nanoparticles immersed in α-MEM followed a similar profile as SBF (Fig. S9). However, dissolution rates of Si were slightly lower in the cell culture medium than in SBF at early time points, which could be explained by the adsorption of proteins present in the cell culture medium forming a permeable coating on the particle surface [46,47]. Ca release was mainly affected by culture media, which resulted in reduced Ca release and a longer precipitation process. The proteins present in the culture medium can adsorb on the glass surface and partially block the pores retarding apatite layer formation [20,46]. It is worth mentioning that the consumption of Ca content of culture media (75 $mg.L^{-1}$ in α-MEM) could be related to the apatite precipitation on nanoparticles resulting in decreasing of Ca concentration to the lower level of the initial value.

3.3. Mineralization capacity of nanoparticles

Once bioactive glass contacts body fluids upon implantation, several interfacial reactions occur as a result of fast ionic exchange leading to the formation of a layer of superficial hydroxyapatite (HA) crystals, which attract various types of biological moieties such as proteins. This HA layer subsequently determines the proliferation and differentiation of osteoblasts, calcification, and eventually bone regeneration [48]. In this study, the in vitro mineralization capacity of the synthesized XCu-PMMBGNs was assessed using FTIR, XRD, and SEM after immersion in SBF for up to 14 days. As shown in Fig. 5A and S10A, a weak shoulder at ~950 cm^{-1} assigned to the non-bridging oxygen ($Si–O_{NBO}$) converted to a slight band at ~970 cm^{-1} after 1 day of immersion as a result of ion

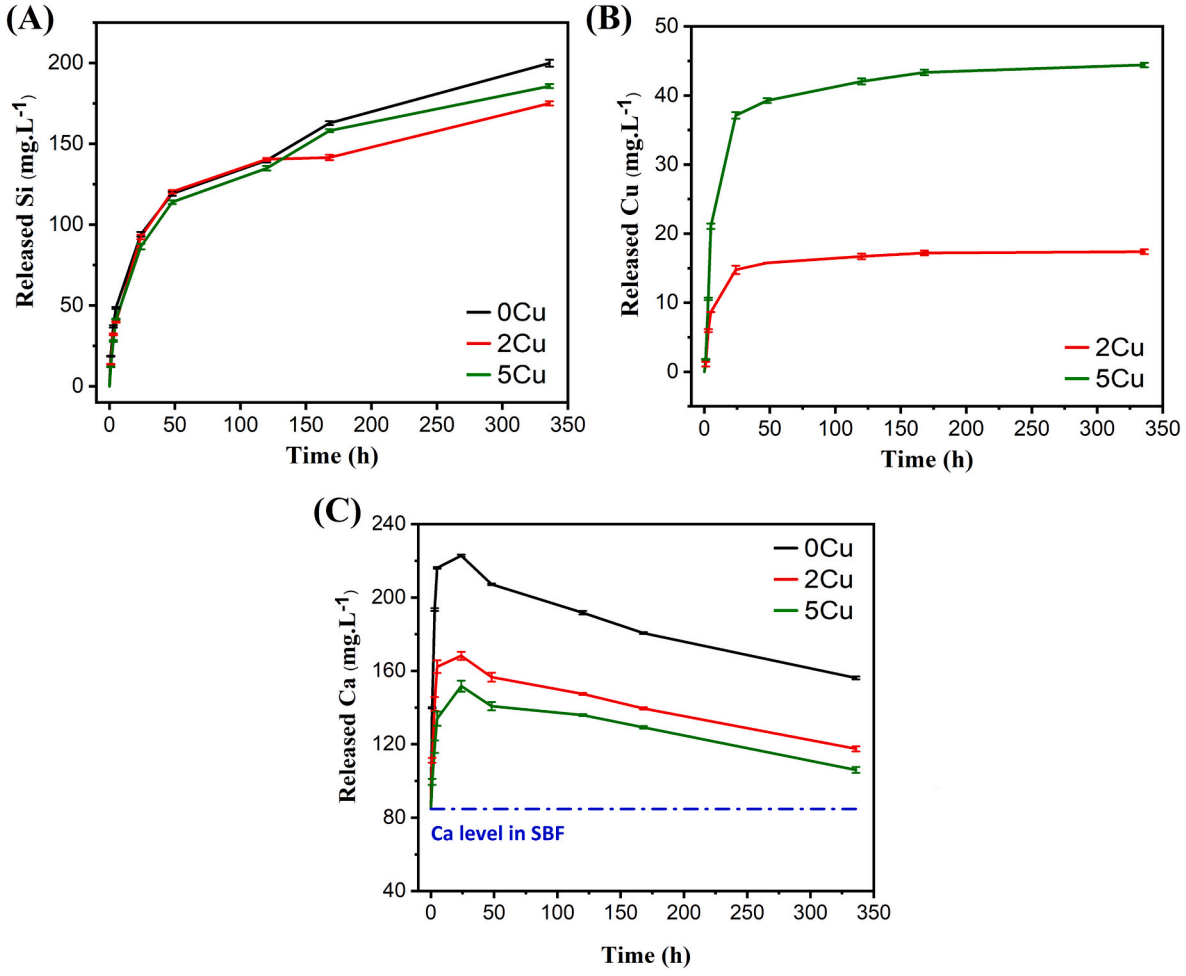

Fig. 4. Dissolution behavior of synthesized nanoparticles. In vitro ion release profiles A) Si, B) Cu, and C) Ca from XCu-PMMBGNs (X = 0, 2, and 5 mol% of Cu) in SBF solution. Dotted horizontal line marks the respective initial concentration of Ca in the SBF solution.

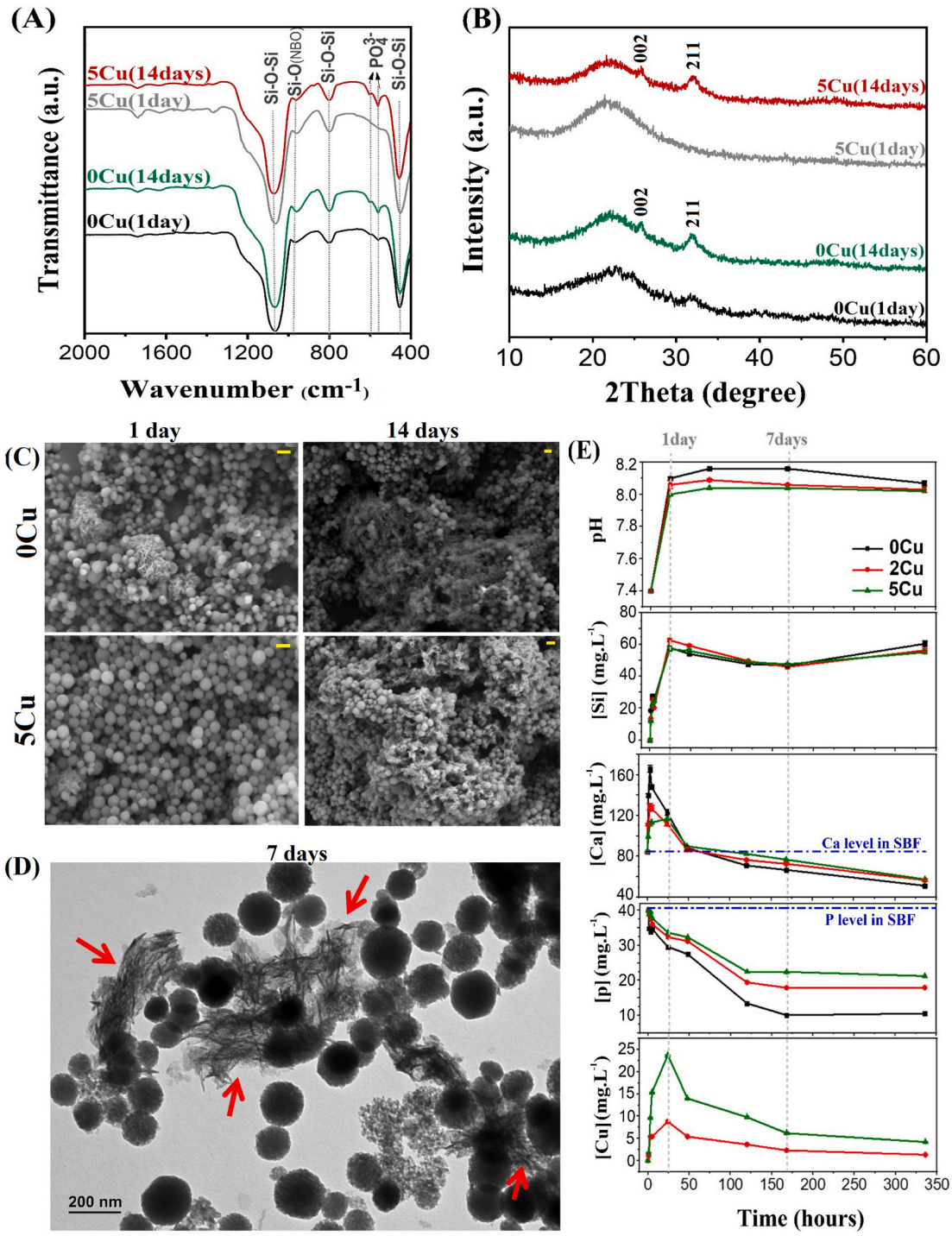

Fig. 5. In vitro mineralization of synthesized XCu-PMMBGNs. A) FTIR spectra and B) XRD patterns of XCu-PMMBGNs (0 and 5 mol% of Cu) after 1 and 14 days of incubation in SBF. C) Representative SEM images of particles after soaking in SBF for 1 and 14 days. D) Representative TEM images of nanoparticles (5Cu-PMMBGNs) after 7 days of soaking in SBF (red arrows indicate HA crystals). E) Kinetics of apatite formation on XCu-PMMBGNs explained by pH change and ion release kinetics for 14 days. The scale bars in SEM images represent 200 nm. (For interpretation of the references to color in this figure legend, the reader is referred to the web version of this article.)

exchange and breakage of Si-O-Si bond. Additionally, a new doublet band at ~560 and ~600 cm^{-1} corresponding to the P−O bending vibration of PO_4^{-3} appeared after immersion for 1 day and 3 days for Cu-free and Cu-containing samples, respectively [20,21]. The deposition of crystalline HA onto the synthesized nanoparticles was confirmed by their XRD patterns (Fig. 5B and S10B). The obvious diffraction peaks at approximately 26.9° and 32°, corresponding to the (002) and (121) crystal planes of hydroxyapatite (JCPD 84-1998), were observed in all samples after immersion for 3 days. Those peaks were intensified with increasing immersion time [49]. Notably, in agreement with FTIR results, Cu-free particles showed more rapid mineralization compared to Cu-containing particles, as HA characteristic peaks appeared already after 1 day of immersion. This rapid HA deposition can be attributed to the higher Ca content in copper-free glasses, leading to higher Ca concentrations and accelerated deposition of calcium phosphate. Moreover, ions with larger radii (Ca) could expand the silica network facilitating

water penetration, ionic exchange, and apatite formation [44]. Figs. 5C and S11 show representative SEM images of copper-free and copper-containing (5 mol%) nanoparticles after immersion in SBF for various time intervals. Needle-like structures, as characteristic apatite morphologies, were observed on the surface of PMMBGNs after prolonged immersion in SBF [20,50,51]. These morphologies are more conspicuous in the corresponding TEM images (Fig. 5D). Collectively, our results are in agreement with previous studies, confirming the mineralization capacity of bioactive glasses.

To have a better understanding of the mechanism and kinetics of the apatite formation process on the XCu-PMMBGNs, we analyzed the changes in Si, Ca, Cu, and P content as well as pH of SBF during the immersion (Fig. 5E). In all samples, the dissolution process starts with Ca ion exchange on the glass surface with hydron (H^+) and hydronium (H_3O^+) ions present in SBF. This leads to a burst release of Ca within the first hours and, as can be seen in Fig. 5E, induces a pH change from 7.4 to 8.2. As a consequence of the ionic exchange, silanol groups (-SiOH) are formed on the glass surface as nucleation sites which favors the apatite layer formation [52,53]. The high pH value accelerates Si-O-Si bond breakage enhancing the release of soluble silica for up to 1 day. Subsequently, more silanol groups are generated on the bioactive glass surface forming a silica-rich layer after the polycondensation process. At the same time, the rapid release of Ca ions through the structures exposed them to PO_4^{3-} species present in SBF. After the saturation stage, Ca and PO_4^{3-} ions present in the solution are adsorbed by a silica-rich layer which subsequently forms a Ca—P layer. As shown in Fig. 5E, a reduction of P concentration in the initial immersion time could confirm the migration of PO_4^{3-} present in SBF to the bioactive glass surface to form the Ca—P layer [54]. Results showed that the release of Si ions stopped after 1 day which is possibly due to the Ca—P precipitation, covering the surface of nanoparticles. The formation of the Ca—P layer was likely slowed down by the time allowing Si ions to be released as before, after 1 week. Results indicate a competition between glass dissolution and Ca—P mineralization.

3.4. Antibacterial properties of nanoparticles

The antibacterial performance of synthesized XCu-PMMBGNs was firstly assessed by directly exposing different concentrations of nanoparticle dispersion with bacterial culture and monitoring the bacterial growth curve for 24 h (Fig. 6A). In this study, multidrug-resistant MRSA was selected as a clinically relevant and major sepsis-causing microorganism responsible for severe bone infections [55]. Additionally, the time delay, induced by nanoparticles, at the start of the log phase, was depicted in Fig. 6B. As shown in Fig. 6A, copper-free nanoparticles (0Cu-PMMBGNs) exhibited a dose-dependent inhibitory effect on bacterial growth. This observation highlights the intrinsic antibacterial properties of bioactive glasses which are attributed to the effect of released ions through the nanoparticles altering the osmotic pressure and local pH (Fig. 5E) [56]. Incorporation of copper ions into the nanoparticles induced retarded log phase in bacterial growth and enhanced their inhibitory effect. Notably, 5Cu-PMMBGNs at a concentration of 500 and 1000 μg.mL^{-1} inhibited bacterial growth to a similar extent as vancomycin (8 μg.mL^{-1}), a well-known effective antibiotic against MRSA

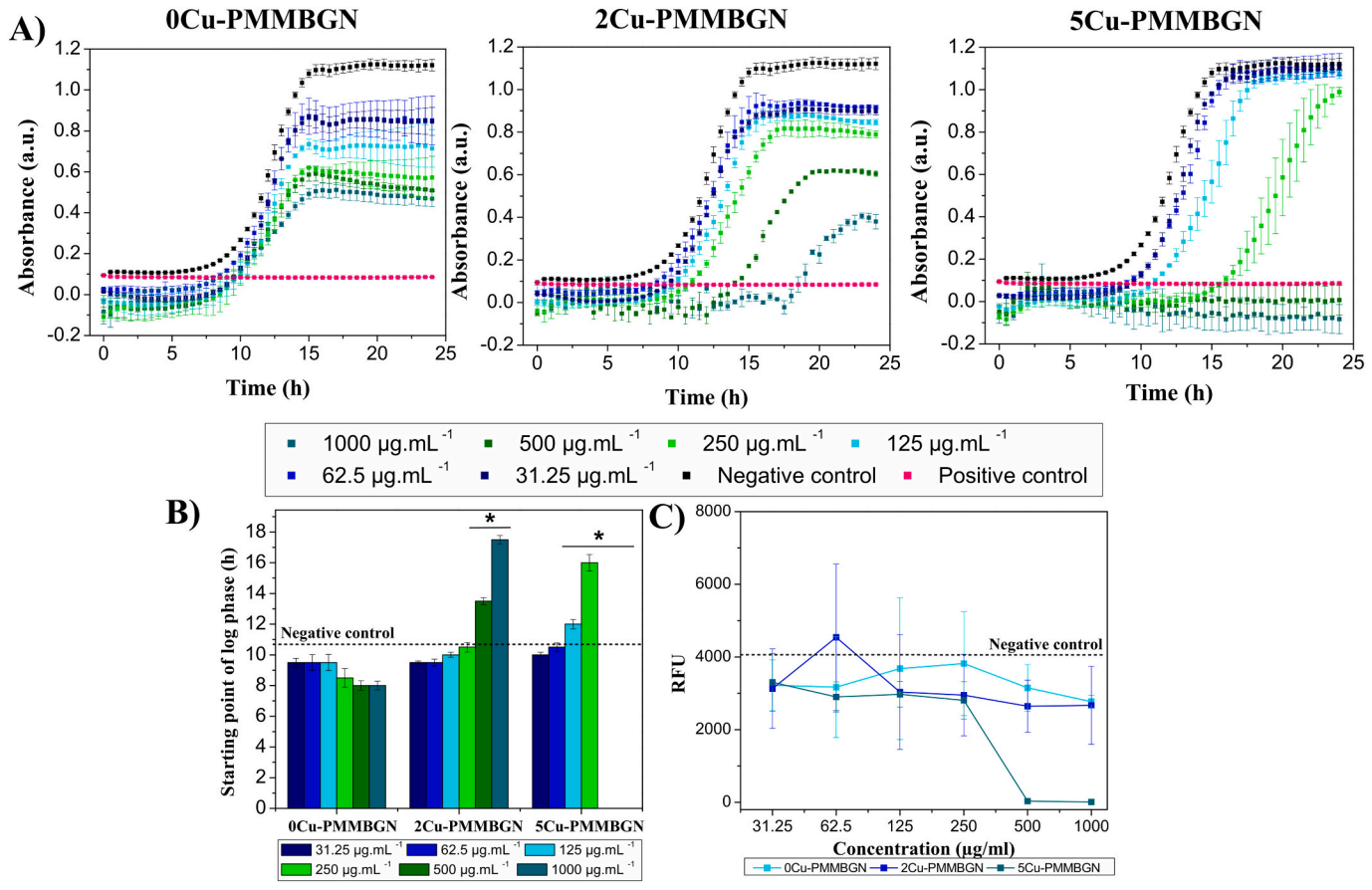

Fig. 6. Antibacterial efficacy of synthesized nanoparticles. A) Growth curve of MRSA bacteria exposed to XCu-PMMBGNs (X = 0, 2, and 5 mol% of Cu) with increasing serial dilution of nanoparticles for 24 h. B) The effect of XCu-PMMBGNs on starting point of bacterial growth. The dashed black line indicates the starting point of bacterial growth without being in contact with nanoparticles. C) MRSA viability in contact with XCu-PMMBGNs with different concentrations for 24 h. The relative fluorescent unit (RFU) of generated resorufin is considered to be proportional to the number of viable bacterial cells. The dashed black line in C indicates the negative control group (Bacteria without nanoparticles).

bacteria [57]. Moreover, the antibacterial properties of synthesized nanoparticles were supported by results from the resazurin assay (Fig. 6C). 5Cu-PMMBGNs at concentrations of 500 and 1000 μg.mL^{-1} showed superior bactericidal properties, evidenced by resorufin signals close to zero which indicate that bacteria were not metabolically active. Among a few studies on the antibacterial effect of copper-containing MBGNs (2 mol%), Bari et al. reported a 50 % growth inhibition of *S. aureus* (8325-4) in contact with 2 mg/mL of nanoparticles for 1 day. This inhibitory effect reached 70–75 % after 3 days of incubation [15]. Li et al. showed that copper ions at concentrations of 37 and 111 μM inhibited *S. aureus* bacterial growth by about 90 and 100 %, respectively [58]. In the present study, the amount of copper released from nanoparticle dispersion was about 217 μM which is higher than the reported value by Li et al. explaining the potent antibacterial effect of 5Cu-PMMBGNs against MRSA bacteria.

In agreement with relevant literature regarding copper-eluting biomaterials, our results demonstrate that the strong antibacterial properties of synthesized nanoparticles against MRSA bacteria are related to the copper ion released from the particles [59–62]. Although the exact antibacterial mechanism of copper ions remains to be elucidated, it is most likely related to the disruption of bacterial cytoplasmic membranes, leading to the leakage of intracellular components like proteins and sugars. Furthermore, exogenous Cu ions can deactivate the respiratory chains and generate high levels of reactive oxygen species (ROS) by catalyzing the Fenton reaction. These ROS cause irreversible oxidative damage to the proteins, lipids, and nucleic acids, and can eventually lead to cell death. More specifically, it has been reported that the exogenous copper ions can significantly disturb the gene replication process in *S. aureus* [63,64]. Taken together, due to the remarkable antibacterial efficacy of the synthesized nanoparticles against MRSA bacteria, utilizing 5Cu-PMMBGNs as an antibacterial component of a bone substitute and evaluating their therapeutic efficacy in vivo are logical steps in our future study.

3.5. Cell viability and internalization of nanoparticles

The synthesized XCu-PMMBGNs are intended for the treatment of infected bone defects, which would entail direct contact with mammalian cells. Therefore, in the present study preosteoblast cells (MC3T3-E1) were exposed to the 5Cu-PMMBGNs for 1 and 3 days at concentrations of 500 and 1000 μg.mL^{-1} as these concentrations showed the most pronounced and effective antibacterial properties against MRSA bacteria. As shown in Fig. 7A, nanoparticles showed a dose-dependent cytotoxic effect on MC3T3-E1 cells. This finding is in line with the observation reported by Zheng et al. for copper-containing MBGNs (7 % mole Cu) produced by the common microemulsion method [20].

After exposure for 1 and 3 days, 5Cu-PMMBGNs at a concentration of 500 μg.mL^{-1} had no significant cytotoxic effect on cells (~85–89 % cell viability, $p > 0.05$) compared to the control group (cells with no treatment). However, a higher concentration of nanoparticles (1000 μg.mL^{-1}) exhibited an obvious cytotoxic effect on cell viability (50–62 % cell viability, $p < 0.05$). This high cytotoxicity could be related to the high content of released ions from the nanoparticles and their accumulation in static conditions [65]. It has been reported that Cu ions above a threshold concentration could induce toxicity toward normal cells. This toxicity can be induced by the formation of abundant hydroxyl radicals as a result of the interaction between superoxide and hydrogen peroxide, in which Cu ions act as a catalyst [66]. Li et al.

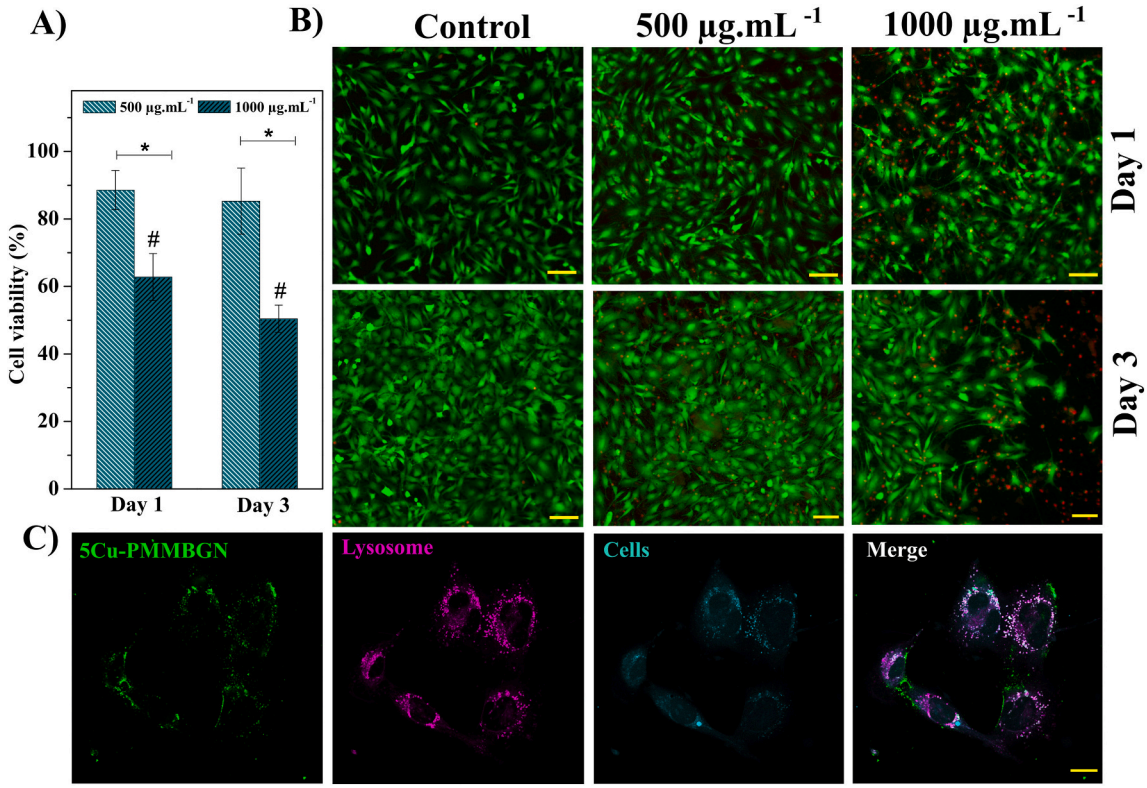

Fig. 7. Interaction between MC3T3-E1 cells and 5Cu-PMMBGNs. A) Quantitative analysis of the cytotoxic effect of 5Cu-PMMBGNs on cell metabolic activity determined by CCK8 assay. * and # indicate a significant difference between 2 different nanoparticle concentrations and control, respectively. B) Representative fluorescence images of the cytotoxic effects of 5Cu-PMMBGNs on the cell viability assessed by live/dead staining. C) LCSM images of 5Cu-PMMBGNs internalized within MC3T3 cells after 24 h. 5Cu-PMMBGNs nanoparticles were labeled with FITC (green). Lysosomes and cells were labeled with LysoTracker Red fluorescent probe (magenta) and CellTrace™ yellow (cyan), respectively. Co-localization of 5Cu-PMMBGNs and lysosomal compartments appears in white. The scale bars in fluorescence and LCSM images represent 100 and 20 μm, respectively. (For interpretation of the references to color in this figure legend, the reader is referred to the web version of this article.)

reported a dose-dependent cytotoxic effect of copper ions against MC3T3-E1 cells and the half maximal inhibitory concentration was about 134.6 μM [58]. Moreover, the representative fluorescent images (live/dead staining) shown in Fig. 7B reflected well the cell viability data. Of note, the samples with lower copper content (2Cu-PMMBGNs) were not included in the cytocompatibility study due to their low efficacy against MRSA. However, their cytotoxicity level might be lower than 5Cu-PMMBGNs due to the lower copper content. Collectively, the cytotoxicity of our synthesized particles correlates with their copper content as well as with particle concentrations, and 5Cu-PMMBGNs at a concentration of 500 $\mu g.mL^{-1}$ could be considered a safe choice for future studies.

The intracellular survival of *Staphylococcus aureus* bacteria along with a weak penetration of available antibiotics into host cell plasma membranes has been recognized as a major factor in the recurrence of infections and associated with therapeutic failures [67]. Therefore, introducing antibacterial agents with a high bactericidal activity along with internalization ability could open up new opportunities for dealing with intracellular bacteria. We further investigated the internalization ability of synthesized 5Cu-PMMBGNs (50 $\mu g.mL^{-1}$) into MC3T3-E1 cells. The cellular uptake of nanoparticles was visualized by labeling nanoparticles using FITC-APTES conjugate (Fig. 7C, green channel). Live cell images reveal abundant internalization of 5Cu-PMMBGNs with their predominant colocalization with lysosomes after 24 h of incubation as shown in Fig. 7C, merged channels. Z-stacking images showed an increase in fluorescence intensity from the surface of the cell, confirming the internalization of the particles and not simply binding to the cell surface (Movie S1). The ability of these nanoparticles as intracellular drug (antibacterial agents) carriers to fight infected cells will be the focus of our future work.

4. Conclusion

Here, we have presented a facile post-modification approach to fabricate antibiotic-free antibacterial copper-containing MBGNs. The incorporation of therapeutic ions (Ca and Cu) into the silica network was facilitated by introducing amine groups as anchoring sites into the MSN surface area and pore volume. This post-surface modification strategy can overcome the main challenges associated with conventional methods such as the microemulsion-assisted sol-gel method to synthesize MBGNs such as i) better control over particle dispersity, ii) incorporation of higher content of calcium and copper ions into the silica network without forming any crystals and disturbing the particle homogeneity, iii) providing a versatile platform to produce a wide range of MBGNs with various sizes, compositions, and (pore) morphologies. The resulting particles had a particle size of ~110 nm and pore size of ~3 nm. Their apatite mineralization capacity was confirmed in vitro upon immersion in SBF after 3 days. Moreover, 5Cu-PMMBGNs could effectively inhibit the growth of clinically relevant bacteria (MRSA) at concentrations of 500 and 1000 $\mu g.mL^{-1}$ as evidenced by a significant reduction (~99.9 %) of bacterial viability after 24 h of incubation. Given the morphological features (e.g., nanoscale properties, mesoporous structure), mineralization capacity, antibacterial properties, and internalization ability, these nanoparticles provide new opportunities for the design of multifunctional biomaterials such as coating or hydrogel composites for the treatment of infected bone defects.

Supplementary data to this article can be found online at https://doi.org/10.1016/j.bioadv.2022.213198.

CRediT authorship contribution statement

Maryam Hosseini: Conceptualization, Methodology, Formal analysis, Investigation, Data curation, Visualization, Writing – original draft, Writing – review & editing. **Negar Hassani Besheli:** Conceptualization, Methodology, Formal analysis, Investigation, Data curation, Visualization, Writing – original draft, Writing – review & editing. **Dongmei Deng:** Methodology, Data curation, Writing – review & editing. **Caroline Lievens:** Methodology, Data curation, Writing – review & editing. **Yi Zuo:** Methodology, Data curation, Writing – review & editing. **Sander C.G. Leeuwenburgh:** Conceptualization, Methodology, Funding acquisition, Supervision, Project administration, Writing – review & editing. **Fang Yang:** Conceptualization, Methodology, Funding acquisition, Supervision, Project administration, Writing – review & editing.

Declaration of competing interest

The authors declare no conflict of interest.

Data availability

The data that support the findings of this study are available from the corresponding author.

Acknowledgments

This work was financially supported by the Radboud Institute for Molecular Life Science (RIMLS) of Radboudumc.

References

[1] R. Dimitriou, E. Jones, D. McGonagle, P.V. Giannoudis, Bone regeneration: current concepts and future directions, BMC Med. 9 (1) (2011) 66.
[2] N. Kavanagh, E.J. Ryan, A. Widaa, G. Sexton, J. Fennell, S. O'Rourke, K.C. Cahill, C.J. Kearney, F.J. O'Brien, S.W. Kerrigan, Staphylococcal osteomyelitis: disease progression, treatment challenges, and future directions, Clin. Microbiol. Rev. 31 (2) (2018), e00084-17.
[3] Y.-C. Yeh, T.-H. Huang, S.-C. Yang, C.-C. Chen, J.-Y. Fang, Nano-based drug delivery or targeting to eradicate bacteria for infection mitigation: a review of recent advances, Front. Chem. 8 (2020) 286.
[4] J.A.P. Geurts, T.A.G. van Vugt, J.J.C. Arts, Use of contemporary biomaterials in chronic osteomyelitis treatment: clinical lessons learned and literature review, J. Orthop. Res. 39 (2) (2021) 258–264.
[5] J.A. Inzana, E.M. Schwarz, S.L. Kates, H.A. Awad, Biomaterials approaches to treating implant-associated osteomyelitis, Biomaterials 81 (2016) 58–71.
[6] S.B. Levy, B. Marshall, Antibacterial resistance worldwide: causes, challenges and responses, Nat. Med. 10 (12) (2004) S122–S129.
[7] J.C. Dombrowski, L.G. Winston, Clinical failures of appropriately-treated methicillin-resistant Staphylococcus aureus infections, J. Infect. 57 (2) (2008) 110–115.
[8] Y. Gao, Y. Chen, Y. Cao, A. Mo, Q. Peng, Potentials of nanotechnology in treatment of methicillin-resistant Staphylococcus aureus, Eur. J. Med. Chem. 213 (2021), 113056.
[9] S. Kargozar, M. Montazerian, S. Hamzehlou, H.-W. Kim, F. Baino, Mesoporous bioactive glasses: promising platforms for antibacterial strategies, Acta Biomater. 81 (2018) 1–19.
[10] M. Vallet-Regi, A.J. Salinas, Mesoporous bioactive glasses for regenerative medicine, Mater. Today Bio 11 (2021), 100121.
[11] C. Wu, J. Chang, Mesoporous bioactive glasses: structure characteristics, drug/growth factor delivery and bone regeneration application, Interface Focus 2 (3) (2012) 292–306.
[12] C. Zhao, W. Liu, M. Zhu, C. Wu, Y. Zhu, Bioceramic-based scaffolds with antibacterial function for bone tissue engineering: a review, Bioact. Mater. 18 (2022) 383–398.
[13] S. Akhtach, Z. Tabia, M. Bricha, K. El Mabrouk, Structural characterization, in vitro bioactivity, and antibacterial evaluation of low silver-doped bioactive glasses, Ceram. Int. 47 (20) (2021) 29036–29046.
[14] P. Wang, Y. Yuan, K. Xu, H. Zhong, Y. Yang, S. Jin, K. Yang, X. Qi, Biological applications of copper-containing materials, Bioact. Mater. 6 (4) (2021) 916–927.
[15] A. Bari, N. Bloise, S. Fiorilli, G. Novajra, M. Vallet-Regí, G. Bruni, A. Torres-Pardo, J.M. González-Calbet, L. Visai, C. Vitale-Brovarone, Copper-containing mesoporous bioactive glass nanoparticles as multifunctional agent for bone regeneration, Acta Biomater. 55 (2017) 493–504.
[16] F. Kurtuldu, N. Mutlu, M. Michálek, K. Zheng, M. Masar, L. Liverani, S. Chen, D. Galusek, A.R. Boccaccini, Cerium and gallium containing mesoporous bioactive glass nanoparticles for bone regeneration: bioactivity, biocompatibility and antibacterial activity, Mater. Sci. Eng. C. 124 (2021), 112050.
[17] Q. Liang, Q. Hu, G. Miao, B. Yuan, X. Chen, A facile synthesis of novel mesoporous bioactive glass nanoparticles with various morphologies and tunable mesostructure by sacrificial liquid template method, Mater. Lett. 148 (2015) 45–49.
[18] Q. Nawaz, M.A.U. Rehman, A. Burkovski, J. Schmidt, A.M. Beltrán, A. Shahid, N. K. Alber, W. Peukert, A.R. Boccaccini, Synthesis and characterization of manganese containing mesoporous bioactive glass nanoparticles for biomedical applications, J. Mater. Sci. Mater. Med. 29 (5) (2018) 64.
[19] F. Westhauser, S. Wilkesmann, Q. Nawaz, F. Hohenbild, F. Rehder, M. Saur, J. Fellenberg, A. Moghaddam, M.S. Ali, W. Peukert, A.R. Boccaccini, Effect of

manganese, zinc, and copper on the biological and osteogenic properties of mesoporous bioactive glass nanoparticles, J. Biomed. Mater. Res. A 109 (8) (2021) 1457–1467.
[20] K. Zheng, J. Kang, B. Rutkowski, M. Gawęda, J. Zhang, Y. Wang, N. Founier, M. Sitarz, N. Taccardi, A.R. Boccaccini, Toward highly dispersed mesoporous bioactive glass nanoparticles with high Cu concentration using Cu/ascorbic acid complex as precursor, Front. Chem. 7 (497) (2019).
[21] K. Zheng, P. Balasubramanian, T.E. Paterson, R. Stein, S. MacNeil, S. Fiorilli, C. Vitale-Brovarone, J. Shepherd, A.R. Boccaccini, Ag modified mesoporous bioactive glass nanoparticles for enhanced antibacterial activity in 3D infected skin model, Mater. Sci. Eng. C. 103 (2019), 109764.
[22] S.L. Greasley, S.J. Page, S. Sirovica, S. Chen, R.A. Martin, A. Riveiro, J.V. Hanna, A. E. Porter, J.R. Jones, Controlling particle size in the Stöber process and incorporation of calcium, J. Colloid Interface Sci. 469 (2016) 213–223.
[23] P. Naruphontjirakul, S.L. Greasley, S. Chen, A.E. Porter, J.R. Jones, Monodispersed strontium containing bioactive glass nanoparticles and MC3T3-E1 cellular response, Biomed. Glas. 2 (1) (2016) 72–81.
[24] C. Wang, Y. Xie, A. Li, H. Shen, D. Wu, D. Qiu, Bioactive nanoparticle through postmodification of colloidal silica, ACS Appl. Mater. Interfaces 6 (7) (2014) 4935–4939.
[25] D. Kozon, K. Zheng, E. Boccardi, Y. Liu, L. Liverani, A.R. Boccaccini, Synthesis of monodispersed Ag-doped bioactive glass nanoparticles via surface modification, Materials 9 (4) (2016) 225 (Basel, Switzerland).
[26] E. Da'na, A. Sayari, Adsorption of heavy metals on amine-functionalized SBA-15 prepared by co-condensation: applications to real water samples, Desalination 285 (2012) 62–67.
[27] W. Naowanon, R. Chueachot, S. Klinsrisuk, S. Amnuaypanich, Biphasic synthesis of amine-functionalized mesoporous silica nanospheres (MSN-NH2) and its application for removal of ferrous (Fe2+) and copper (Cu2+) ions, Powder Technol. 323 (2018) 548–557.
[28] M.P. Daryasari, M.R. Akhgar, F. Mamashli, B. Bigdeli, M. Khoobi, Chitosan-folate coated mesoporous silica nanoparticles as a smart and pH-sensitive system for curcumin delivery, RSC Adv. 6 (107) (2016) 105578–105588.
[29] M. Martínez-Carmona, Q.P. Ho, J. Morand, A. García, E. Ortega, L.C.S. Erthal, E. Ruiz-Hernandez, M.D. Santana, J. Ruiz, M. Vallet-Regí, Y.K. Gun'ko, Amino-functionalized mesoporous silica nanoparticle-encapsulated octahedral organoruthenium complex as an efficient platform for combatting cancer, Inorg. Chem. 59 (14) (2020) 10275–10284.
[30] M.V. Cabañas, D. Lozano, A. Torres-Pardo, C. Sobrino, J. González-Calbet, D. Arcos, M. Vallet-Regí, Features of aminopropyl modified mesoporous silica nanoparticles. Implications on the active targeting capability, Mater. Chem. Phys. 220 (2018) 260–269.
[31] J. Liu, Z. Luo, J. Zhang, T. Luo, J. Zhou, X. Zhao, K. Cai, Hollow mesoporous silica nanoparticles facilitated drug delivery via cascade pH stimuli in tumor microenvironment for tumor therapy, Biomaterials 83 (2016) 51–65.
[32] A.L. Maçon, T.B. Kim, E.M. Valliant, K. Goetschius, R.K. Brow, D.E. Day, A. Hoppe, A.R. Boccaccini, I.Y. Kim, C. Ohtsuki, T. Kokubo, A. Osaka, M. Vallet-Regí, D. Arcos, L. Fraile, A.J. Salinas, A.V. Teixeira, Y. Vueva, R.M. Almeida, M. Miola, C. Vitale-Brovarone, E. Verné, W. Höland, J.R. Jones, A unified in vitro evaluation for apatite-forming ability of bioactive glasses and their variants, J. Mater. Sci. Mater. Med. 26 (2) (2015) 115.
[33] T. Kokubo, H. Takadama, How useful is SBF in predicting in vivo bone bioactivity? Biomaterials 27 (15) (2006) 2907–2915.
[34] H. Gu, Y. Guo, S.Y. Wong, Z. Zhang, X. Ni, Z. Zhang, W. Hou, C. He, V.P.W. Shim, X. Li, Study of amino-functionalized mesoporous silica nanoparticles (NH2-MSN) and polyamide-6 nanocomposites co-incorporated with NH2-MSN and organo-montmorillonite, Microporous Mesoporous Mater. 170 (2013) 226–234.
[35] N.S. Zaharudin, E.D. Mohamed Isa, H. Ahmad, M.B. Abdul Rahman, K. Jumbri, Functionalized mesoporous silica nanoparticles templated by pyridinium ionic liquid for hydrophilic and hydrophobic drug release application, J. Saudi Chem. Soc. 24 (3) (2020) 289–302.
[36] S. Lin, C. Ionescu, K.J. Pike, M.E. Smith, J.R. Jones, Nanostructure evolution and calcium distribution in sol–gel derived bioactive glass, J. Mater. Chem. 19 (9) (2009) 1276–1282.
[37] B.J. Madhu, H. Bhagyalakshmi, B. Shruthi, M. Veerabhadraswamy, Structural, AC conductivity, dielectric and catalytic behavior of calcium oxide nanoparticles derived from waste eggshells, SN Appl. Sci. 3 (6) (2021) 637.
[38] F. Sameri, A. Mobinikhaledi, M.A. Bodaghifard, High-efficient synthesis of 2-imino-2H-chromenes and dihydropyrano[c]chromenes using novel and green catalyst (CaO@SiO2@AIL), Res. Chem. Intermed. 47 (2) (2021) 723–741.
[39] A. Lesbani, P. Tamba, R. Mohadi, F. Fahmariyanti, Preparation of calcium oxide from Achatina fulica as catalyst for production of biodiesel from waste cooking oil, Indones. J. Chem. 13 (2) (2013) 176–181.
[40] Z. Neščáková, K. Zheng, L. Liverani, Q. Nawaz, D. Galusková, H. Kaňková, M. Michálek, D. Galusek, A.R. Boccaccini, Multifunctional zinc ion doped sol – gel derived mesoporous bioactive glass nanoparticles for biomedical applications, Bioact. Mater. 4 (2019) 312–321.
[41] K. Zheng, E. Torre, A. Bari, N. Taccardi, C. Cassinelli, M. Morra, S. Fiorilli, C. Vitale-Brovarone, G. Iviglia, A.R. Boccaccini, Antioxidant mesoporous Ce-doped bioactive glass nanoparticles with anti-inflammatory and pro-osteogenic activities, Mater.Today Bio 5 (2020), 100041.
[42] M. Anbia, K. Kargosha, S. Khoshbooei, Heavy metal ions removal from aqueous media by modified magnetic mesoporous silica MCM-48, Chem. Eng. Res. Des. 93 (2015) 779–788.
[43] C. Xu, Y. Shan, M. Bilal, B. Xu, L. Cao, Q. Huang, Copper ions chelated mesoporous silica nanoparticles via dopamine chemistry for controlled pesticide release regulated by coordination bonding, Chem. Eng. J. 395 (2020), 125093.
[44] R. Brückner, M. Tylkowski, L. Hupa, D.S. Brauer, Controlling the ion release from mixed alkali bioactive glasses by varying modifier ionic radii and molar volume, J. Mater. Chem. B 4 (18) (2016) 3121–3134.
[45] Z. Tabia, K. El Mabrouk, M. Bricha, K. Nouneh, Mesoporous bioactive glass nanoparticles doped with magnesium: drug delivery and acellular in vitro bioactivity, RSC Adv. 9 (22) (2019) 12232–12246.
[46] S. Lin, J.R. Jones, The effect of serum proteins on apatite growth for 45S5 bioglass and common sol-gel derived glass in SBF, Biomed. Glas. 4 (1) (2018) 13–20.
[47] P. Sepulveda, J.R. Jones, L.L. Hench, In vitro dissolution of melt-derived 45S5 and sol-gel derived 58S bioactive glasses, J. Biomed. Mater. Res. 61 (2) (2002) 301–311.
[48] L.L. Hench, N. Roki, M.B. Fenn, Bioactive glasses: importance of structure and properties in bone regeneration, J. Mol. Struct. 1073 (2014) 24–30.
[49] S.J. Shih, W.L. Tzeng, R. Jatnika, C.J. Shih, K.B. Borisenko, Control of Ag nanoparticle distribution influencing bioactive and antibacterial properties of Ag-doped mesoporous bioactive glass particles prepared by spray pyrolysis, J Biomed Mater Res B Appl Biomater 103 (4) (2015) 899–907.
[50] J. Jiménez-Holguín, S. Sánchez-Salcedo, M. Vallet-Regí, A.J. Salinas, Development and evaluation of copper-containing mesoporous bioactive glasses for bone defects therapy, Microporous Mesoporous Mater. 308 (2020), 110454.
[51] K. Zheng, X. Dai, M. Lu, N. Hüser, N. Taccardi, A.R. Boccaccini, Synthesis of copper-containing bioactive glass nanoparticles using a modified Stöber method for biomedical applications, Colloids Surf. B: Biointerfaces 150 (2017) 159–167.
[52] G. Kaur, G. Pickrell, N. Sriranganathan, V. Kumar, D. Homa, Review and the state of the art: sol-gel and melt quenched bioactive glasses for tissue engineering, J Biomed Mater Res B Appl Biomater 104 (6) (2016) 1248–1275.
[53] J.R. Jones, Review of bioactive glass: from Hench to hybrids, Acta Biomater. 9 (1) (2013) 4457–4486.
[54] M. Diba, J. An, S. Schmidt, M. Hembury, D. Ossipov, A.R. Boccaccini, S. C. Leeuwenburgh, Exploiting bisphosphonate-bioactive-glass interactions for the development of self-healing and bioactive composite hydrogels, Macromol. Rapid Commun. 37 (23) (2016) 1952–1959.
[55] E.A. Masters, R.P. Trombetta, K.L. de Mesy Bentley, B.F. Boyce, A.L. Gill, S.R. Gill, K. Nishitani, M. Ishikawa, Y. Morita, H. Ito, S.N. Bello-Irizarry, M. Ninomiya, J. D. Brodell, C.C. Lee, S.P. Hao, I. Oh, C. Xie, H.A. Awad, J.L. Daiss, J.R. Owen, S. L. Kates, E.M. Schwarz, G. Muthukrishnan, Evolving concepts in bone infection: redefining "biofilm","acute vs. chronic osteomyelitis", "the immune proteome" and "local antibiotic therapy", Bone Res. 7 (1) (2019) 20.
[56] J.S. Fernandes, P. Gentile, R.A. Pires, R.L. Reis, P.V. Hatton, Multifunctional bioactive glass and glass-ceramic biomaterials with antibacterial properties for repair and regeneration of bone tissue, Acta Biomater. 59 (2017) 2–11.
[57] E.J. Choo, H.F. Chambers, Treatment of methicillin-resistant Staphylococcus aureus bacteremia, Infect. Chemother. 48 (4) (2016) 267–273.
[58] K. Li, C. Xia, Y. Qiao, X. Liu, Dose-response relationships between copper and its biocompatibility/antibacterial activities, J. Trace Elem. Med. Biol. 55 (2019) 127–135.
[59] I. Burghardt, F. Lüthen, C. Prinz, B. Kreikemeyer, C. Zietz, H.G. Neumann, J. Rychly, A dual function of copper in designing regenerative implants, Biomaterials 44 (2015) 36–44.
[60] Y. Li, L. Liu, P. Wan, Z. Zhai, Z. Mao, Z. Ouyang, D. Yu, Q. Sun, L. Tan, L. Ren, Z. Zhu, Y. Hao, X. Qu, K. Yang, K. Dai, Biodegradable Mg-Cu alloy implants with antibacterial activity for the treatment of osteomyelitis: in vitro and in vivo evaluations, Biomaterials 106 (2016) 250–263.
[61] Y. Lu, L. Li, Y. Zhu, X. Wang, M. Li, Z. Lin, X. Hu, Y. Zhang, Q. Yin, H. Xia, C. Mao, Multifunctional copper-containing carboxymethyl chitosan/alginate scaffolds for eradicating clinical bacterial infection and promoting bone formation, ACS Appl. Mater. Interfaces 10 (1) (2018) 127–138.
[62] E.J. Ryan, A.J. Ryan, A. González-Vázquez, A. Philippart, F.E. Ciraldo, C. Hobbs, V. Nicolosi, A.R. Boccaccini, C.J. Kearney, F.J. O'Brien, Collagen scaffolds functionalised with copper-eluting bioactive glass reduce infection and enhance osteogenesis and angiogenesis both in vitro and in vivo, Biomaterials 197 (2019) 405–416.
[63] S. Mathews, M. Hans, F. Mücklich, M. Solioz, Contact killing of bacteria on copper is suppressed if bacterial-metal contact is prevented and is induced on iron by copper ions, Appl. Environ. Microbiol. 79 (8) (2013) 2605–2611.
[64] M. Vincent, R.E. Duval, P. Hartemann, M. Engels-Deutsch, Contact killing and antimicrobial properties of copper, J. Appl. Microbiol. 124 (5) (2018) 1032–1046.
[65] F.E. Ciraldo, E. Boccardi, V. Melli, F. Westhauser, A.R. Boccaccini, Tackling bioactive glass excessive in vitro bioreactivity: preconditioning approaches for cell culture tests, Acta Biomater. 75 (2018) 3–10.
[66] Y. Lin, W. Xiao, B.S. Bal, M.N. Rahaman, Effect of copper-doped silicate 13–93 bioactive glass scaffolds on the response of MC3T3-E1 cells in vitro and on bone regeneration and angiogenesis in rat calvarial defects in vivo, Mater. Sci. Eng. C 67 (2016) 440–452.
[67] N.F. Kamaruzzaman, S. Kendall, L. Good, Targeting the hard to reach: challenges and novel strategies in the treatment of intracellular bacterial infections, Br. J. Pharmacol. 174 (14) (2017) 2225–2236.